CFD simulations of blade damage effect on the performance of a transonic axial compressor near stall

Yan-Ling Li[a,*], Abdulnaser Sayma[b]

[a]*Thermo-Fluid Mechanics Research Centre, University of Sussex, Brighton, United Kingdom*
[b]*Department of Mechanical and Aeronautical Engineering, City University London, United Kingdom*

Abstract

Gas turbine axial compressor blades may encounter damage during service for various reasons such as damage by debris from casing or foreign objects impacting the blades, typically near the rotor's tip. This may lead to deterioration of performance and reduction in the surge margin. The damage breaks the cyclic symmetry of the rotor assembly thus computational fluid dynamics (CFD) simulations have to be performed using full annulus compressor assembly. Moreover, downstream boundary conditions are unknown during rotating stall or surge and simulations become difficult.

This paper presents unsteady CFD analyses of compressor performance with tip curl damage. Computations were performed near the stall boundary. The primary objectives are to understand the effect of the damage on the flow behaviour and compressor stability. Computations for the undamaged rotor assembly were also performed as a reference case. A transonic axial

*Corresponding author
Email address:* yanling.m.li@gmail.com (Yan-Ling Li)

compressor rotor was used for the time-accurate numerical unsteady flow simulations, with a variable area nozzle downstream simulating an experimental throttle. Computations were performed at 60% of the rotor design speed. Two different degrees of damage for one blade and multiple damaged blades were investigated. Rotating stall characteristics differ including the number of stall cells, propagation speed and rotating stall cell characteristics. Contrary to expectations, damaged blades with typical degrees of damage do not show noticeable effects on the global compressor performance near stall.

1. Introduction

Compressor performance plays an important role in gas turbine engines. It is normally characterised by pressure rise versus mass flow function as shown in Figure 1. The operating range of the compressor is bounded by the choke and surge boundaries at a given rotational speed. The surge margin indicates how close the operating condition of a compressor is to the surge line. Flow under most of the operating conditions on the map is normally steady in the rotor's frame of reference and axisymmetric. When compressors operate near the surge boundary, mass flow is reduced due to high positive incidence. When the incidence is beyond the critical value, instability may be encountered in the form of flow separation. If the situation gets worse,

it could lead to surge. Surge is a global phenomenon, which is normally characterised by large mass flow and pressure fluctuations or flow reversal. Two types of surge are commonly reported in the literature: classic surge and deep surge. Classic surge normally occurs with large periodic oscillations of mass flow and pressure while deep surge is a more severe phenomena that could lead to flow reversal. More details regarding the classification of surge can be found in Greitzer [1] and de Jager [2].
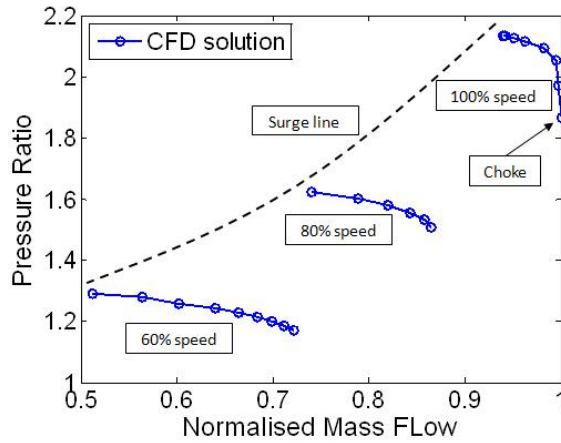
Figure 1: Part of characteristic map of NASA Rotor 37

Another phenomenon compressors normally encounter before surge is rotating stall, which is the focus of this study. It is commonly associated with blade vibrations and at extreme conditions can lead to component failure. Compared to surge, rotating stall is a localised phenomenon to a particular rotor in which a compressor could operate without failure and may recover. It consists of one or more stall cells covering one or more blade passages that propagate in the same direction of the rotor rotation at some fraction of the

3

shaft speed. The number of stall cells and the propagation speed may vary at different operating conditions in different compressors, but typically, the propagation speed is around half of the shaft speed. Rotating stall initiation mechanisms and characteristics are still the subject of continuous scientific debate. However, it generally starts with a localised flow perturbation which causes flow separation on one or more blades due to excessive positive incidence as shown in Figure 2 Iura et al. [3]. The flow separation on the suction side resulting in the formation of a stall cell which reduces the flow passing into the passage. Then the blockage diverts flow around the blade so that the incidence increases on the blade on the right hand side and decreases on the blade on the left hand side, in the rotating frame of reference. This leads to the stall cell moving to the passage to the right. This is the start of propagation of stall cells around the annulus.
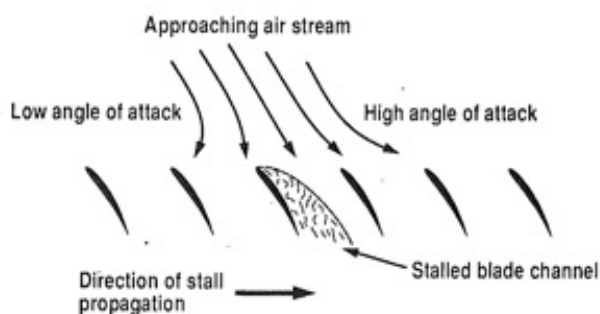

Figure 2: Typical stall cells propagation in an axial compressor [3]

There are two well-known routes leading to rotating stall reported by Vo et al. [4]. One is initiated by a long length-scale or modal inception and the

other starts from a short length-scale or spike inception, distinguished by the type of initial disturbances in pressure or velocity signals. Modal inception normally has a small amplitude disturbance with wavelength seen in the pressure/velocity time histories and requires a large number of revolutions to develop. Spike inception normally has larger amplitudes with a propagation speed of 70-80% of the rotor speed. Spike initiated rotating stall is predicted in this paper.

Although investigations on roating stall drew attention since the 1950's and a lot of work in this area has been done so far, surge and/or rotating stall continue to occur for the reasons such as blade damage, as reported by Levine [5]. Compressor blades may encounter damage during service for various reasons such as loose casing liner, Foreign Object Damage (FOD) or ice formation at the intake. FOD from other sources, such as tire fragments, injection of bird (bird strike) and runaway debris or animals, may also be encountered. This may results in deterioration of the compressor performance and in extreme conditions, may cause compressor instability. During the design process, it is important to be able to predict the aerodynamic behaviour of the compressor in such events to enable the design of robust blades capable of coping with these events.

A literature search showed that the aerodynamic effects for blade-damaged compressors have been overlooked. Most of the available material is about fan blades damaged by bird strike. A 3D simulation of a bird-damaged aero-engine fan assembly was investigated by Kim et al. [6]. The fan assembly

5

was investigated using two damaged blades with different degrees of damage. It was found that flutter stability was reduced and stall was observed at higher mass flow compared to the undamaged fan.

Another investigation by Frischbier et al. [7] using advanced numerical methods was reported on bird ingestion in a multistage turbofan. However, the results showed that the model could not correctly predict the fluid mass going into the low pressure compressor. Recent studies using the commercial code ANSYS/LS-DYNA by Meguid et al. [8] and Guan et al. [9] focused on analysis of structural deformation of fan blades caused by bird strike and no aerodynamic studies were attempted.

A study of the performance, forced response and surge caused by ice-damaged blades in Intermediate Pressure (IP) compressor assemblies was reported by Dhandapani et al. [10]. Results showed that the surge margin was reduced by increasing the number of damaged blades and the severity of performance degradation depended on both the number of damaged blades and their distribution around the annulus.

An aerodynamics study of the effect of bird strike using NASA Rotor 67 was reported by Bohari et al. [11] using CFD. Two damaged assemblies were simulated at different rotational speeds. It was found that the surge margin deteriorated at higher rotational speeds and stall was observed before reaching the working line for both assemblies.

The main objective of this paper is to investigate flow characteristics of rotating stall in axial flow compressors with particular emphasis on the effects

of blade damage on their performance.

2. Description of the compressor

A transonic axial compressor, NASA Rotor 37, was chosen for this study because of the availability of geometry and experimental data in the public domain that can be used for numerical model validation. The rotor was designed as the inlet rotor for a core compressor of an aircraft engine at NASA Lewis Research Centre in the late 1970 's. The rotor has 36 multiple-circular-arc (MCA) blades, a tip speed of 454.14 m/s and a design pressure ratio of 2.106 at the mass flow rate of 20.19 kg/s with an isentropic efficiency of 87.7%. The inlet relative Mach number is 1.13 at the hub and 1.48 at the tip at the design speed of 17,188.7 rpm. The rotor blade has a hub-tip ratio of 0.7, an aspect ratio of 1.19, and tip solidity of 1.288. The tip clearance at design speed is 0.356 mm. The main specifications of the compressor are listed in Table 1 [12].

3. Numerical methodology

3.1. The 3D flow solver

The CFD code used in this investigation is an in-house code, SURF, which is an implicit time accurate 3D compressible solver based on the methodology developed by Sayma et al. [13]. It uses an edge-based data structure for computational efficiency. The model solves the viscous compressible Reynolds-

Rotor inlet hub to tip diameter ratio	0.7
Rotor blade aspect ratio	1.19
Rotor tip relative inlet Mach number	1.48
Rotor hub relative inlet Mach number	1.13
Rotor tip solidity	1.29
Blade airfoil sections	MCA
Number of blades	36
Design wheel speed(rad/s)	1,800
Tip speed (m/s)	454
Rotor total pressure ratio	2.106
Rotor efficiency (adiabatic)	0.877
Measured choking mass flow rate (kg/s)	20.93
Reference temperature (K)	288.15
Reference pressure (kN/m^2)	101.33

Table 1: Specifications of Rotor 37

Averaged Navier-Stokes Equations. The Spalart and Allmaras one-equation turbulence model was used in this investigation.

A mixture of second- and fourth-order matrix artificial dissipation is applied to stabilise the central difference scheme. For unsteady flow simulations, dual time stepping is applied with an outer Newton iteration procedure where time steps are dictated by the physical constraints and fixed throughout the solution domain. Within the Newton iterations, the solution is advanced to convergence using the traditional acceleration techniques associated with steady state flow solutions [14]. The mesh generation tool provides a semi-unstructured mesh combining the advantages of structured and unstructured meshes. A typical mesh used for the rotor is shown in Figure 3. Tip clearance of the rotor is represented by a constant gap between the blade and

the casing, which is meshed allowing the flow to pass over the tip. The tip clearance used in this paper is the same as the one obtained from the experiment at 60% of design speed [15]. Because the flow equations are solved in a rotating frame of reference, the grid points on the casing are given zero rotational speed. Hence, it is inherently assumed that a given blade sees the same mesh points on the casing all the time.
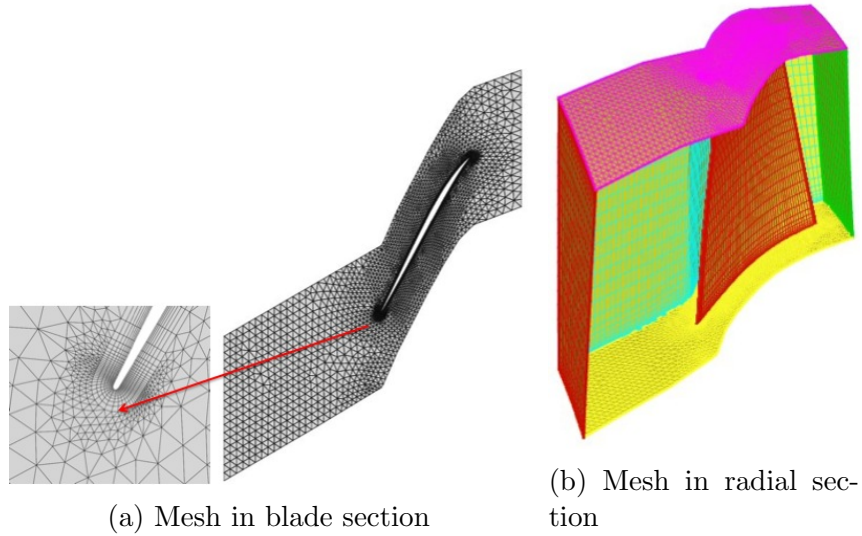

(a) Mesh in blade section

(b) Mesh in radial section

Figure 3: Typical mesh used for Rotor 37

3.2. Computational geometry and solution domain

The method used to initiate stall involved gradually throttling the operating point up to the stability limit using steady state simulations. Then unsteady computations started from solutions obtained from the steady state simulations. The domain for steady state computations is shown in Figure 4. It consists of a rotor, an outlet guide vane (OGV) and a variable nozzle. The

OGV was used to remove the flow swirl downstream of the rotor. Mixing planes were used between blade rows for the steady state simulations. Since the axisymmetry of the flow will be broken by rotating stall, it is desirable to be simulated with a full annulus model. The assembly used in unsteady computations consists of the same components used in the steady state analysis, but in full annulus fashion which is shown in Figure 5. Sliding planes were used at the interfaces of the blade rows instead. Most of the unsteady simulations were performed by introducing damaged blades into the rotor assembly. The corresponding computational domain contains about 10 million grid points.

Figure 4: Model for steady state computation

A major difficulty in rotating stall simulations is to specify the downstream boundary conditions when there are fluctuations in mass flow and pressure rise. In this investigation, a methodology reported by Vahdati et al. [16] using a choked nozzle to control downstream flow boundary conditions was used. The inlet boundary is located at about three chord lengths upstream of the rotor blade. At the inlet, ambient conditions were assumed and uniform total pressure and temperature were applied. The nozzle has a length of approximately eight chord lengths of the rotor blade, as shown in
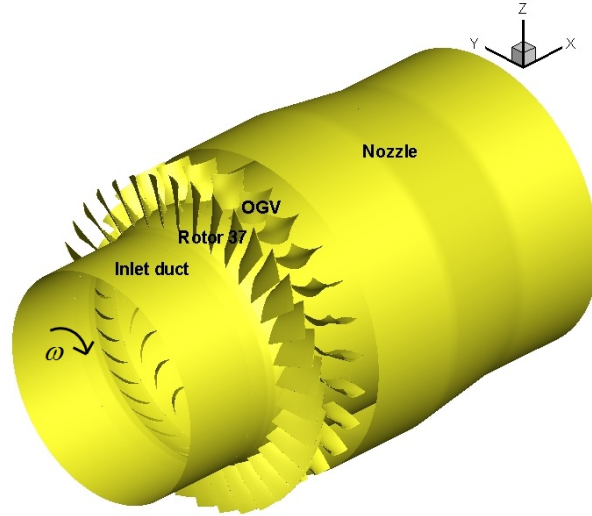
10

Figure 5: Representing model for unsteady time accurate simulations

Figure 4. Different performance points on the compressor characteristic map can be achieved by adjusting the size of the downstream nozzle with a constant back pressure. If fixed static pressure profile is provided downstream of the compressor, the flow is stable under most of the operating conditions. However, numerical difficulties could be encountered when the compressor is approaching stall where the downstream boundary conditions are neither known nor fixed. Therefore, this approach could provide better boundary condition for rotating stall studies than prescribed pressure profiles. More details can be found in Wu et al. [17].

4. Model validation

4.1. Grid independence study

It could take a large number of compressor revolutions for rotating stall computations, requiring extensive computational resources. Hence it is important to strike a balance between grid refinement and the required accuracy of the solutions, so that fundamental flow features pertinent to rotating stall are not significantly affected by the grid quality. An extensive investigation was carried out during this study to choose a suitable grid quality for the code validation and unsteady computations. Although the primary purpose of this analysis is to perform unsteady computations, it was only practical to conduct a grid independence study using steady state single passage analysis within limited time scale and available computing resources. Only the main comparisons are presented here, as it is not the main objective of this paper.

The grid independence study was investigated at the design speed for a point close to peak efficiency. Five grids of increased refinement in all directions were used. The number of grid points and a summary of the resulting solutions are shown in Table 2. As seen in the table, the main flow parameters changed very little when the grid was refined gradually. The maximum difference was less than 1%. To examine the flow in detail, a comparison of pressure profiles at 95% span is shown in Figure 6 and comparisons of radial distributions of the circumferentially averaged pressure ratio and temperature ratio are shown in Figure 7. Results show that there is very little difference in these flow features between the grids used, with the

12

differences mainly around the shock and close to hub and tip in the radial profiles. Close examinations of the differences show that they decrease as the grid is refined. Solution on mesh 1 shows the largest difference in most aspects. However the maximum difference in the pressure rise is much less than 1%. Mesh 1 and mesh 5 are also investigated at the near stall condition. The results show that both meshes can capture similar flow pattern and mesh 1 can also capture the key features of the flow near stall. Therefore as limited by the computational costs, it was decided to use mesh 1 for the unsteady simulations, but the steady state code validation results presented in the next subsection were performed on mesh 3.

Case	Mesh 1	Mesh 2	Mesh 3	Mesh 4	Mesh 5
Grid points	165,504	266,421	390,585	608,354	1,224,335
Mass flow (kg/s)	20.5567	20.4583	20.4199	20.4018	20.3998
Pressure ratio	2.097	2.095	2.095	2.095	2.096
Temperature ratio	1.271	1.271	1.271	1.272	1.272
Isentropic efficiency	0.87	0.87	0.87	0.87	0.87

Table 2: Overall performance comparison for five different grids

4.2. Model validation

This subsection presents comparisons between experimental data [15] and CFD simulations. Comparisons of compressor characteristic map at three different rotational speeds are shown in Figure 8. It can be seen that CFD solutions have a good agreement with the experimental data for the pressure ratio. Efficiencies at all three speeds are under predicted. This may be ex-
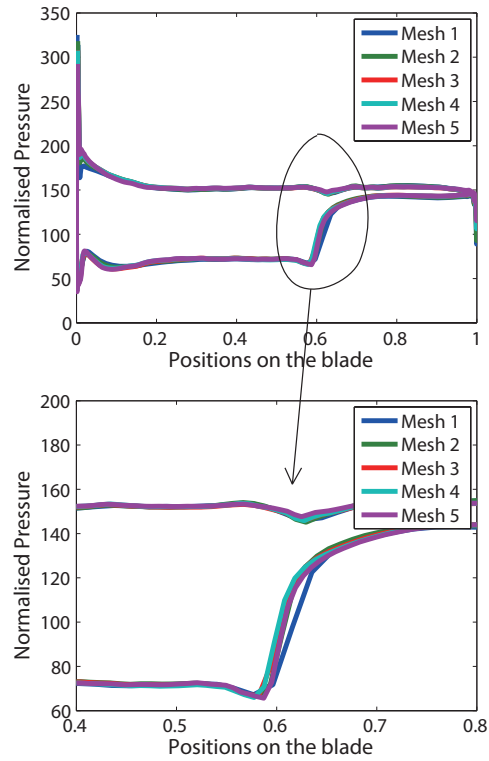
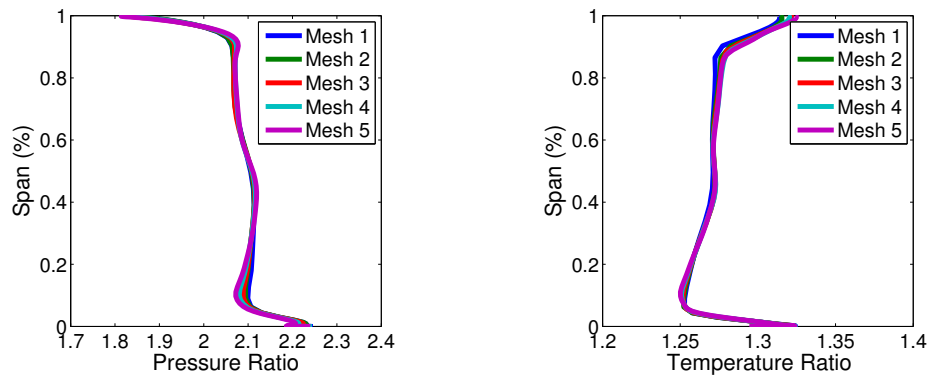Figure 6: Pressure profile comparison at 95% span

Figure 7: Radial distribution of circumferentially averaged pressure and temperature ratios for the rotor

plained firstly by referring to Denton [12]. Measurements do not capture accurately the high loss regions boundary layer due to limitations of the instrumentation, which also explains why the pressure ratio matching is much less affected. Secondly nominal uniform tip clearance values were used for the three speeds in this study, which are likely to have differences from those prevailing during the experiment. In addition, CFD predictions may be affected by the use of wall functions and one-equation turbulence model. A combination of these factors may have contributed to the differences observed in efficiency.

(a) Mass flow versus pressure ratio   (b) Mass flow versus adiabatic efficiency
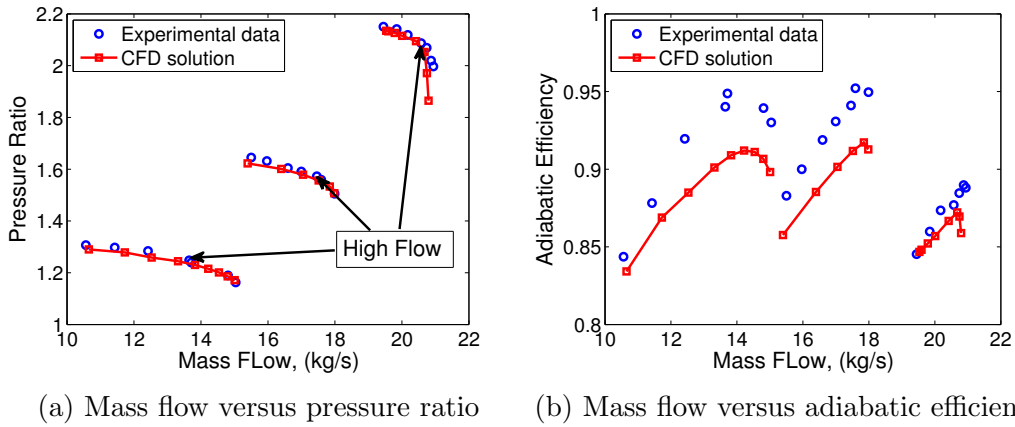
Figure 8: Compressor map comparisons (Right to left: design speed, 80% speed and 60% speed)

Total pressure ratio and temperature ratio distributions in the spanwise direction for the three speeds are shown in Figure 9. The solutions from CFD were circumferentially averaged. Those distributions were obtained at high flow operating conditions, which were marked in the pressure ratio map in Figure 8. The CFD results agree fairly well with the measured quantities.

It can also be seen that the code is capable of predicting a typical pressure deficit at the tip and hub.

These general and detailed agreements between the steady-state solution and experimental data gave confidence in the ability of the code for performing accurate predictions for the present study. Since there was no unsteady experimental data available, further validations using this case were not possible. However, the methodology was previously validated for unsteady simulations (See reference [18]).

5. Results and discussion for unsteady simulations

5.1. Unsteady simulation away from stall condition

All unsteady simulations were performed at 60% of the design speed. The main reason for the choice of this speed is that rotating stall is typically observed at compressor part speed. Before considering the unsteady simulation of rotating stall, it would be useful to look at the flow field and its behaviour when operating away from surge line. To capture the unsteady flow characteristics, eight sets of numerical sensors were located in the stationary frame, positioned about 76% of chord length upstream of leading edge of the rotor. They were placed 45 degrees apart along the circumferential direction. The numerical sensors used for all unsteady cases were located at same locations. 8 numerical sensors at different circumferential positions on the casing will be noted as n1, n2, ..., n8, respectively.
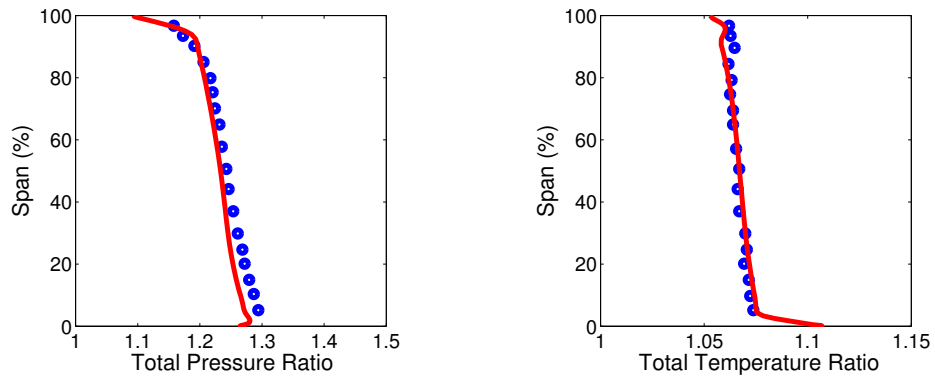
As seen in Figure 10, the pressure fluctuation caused by blade-passing

16
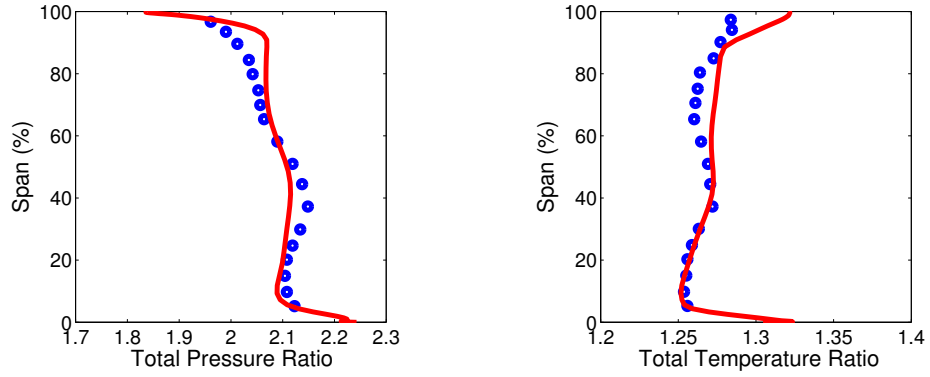
(a) 100% speed
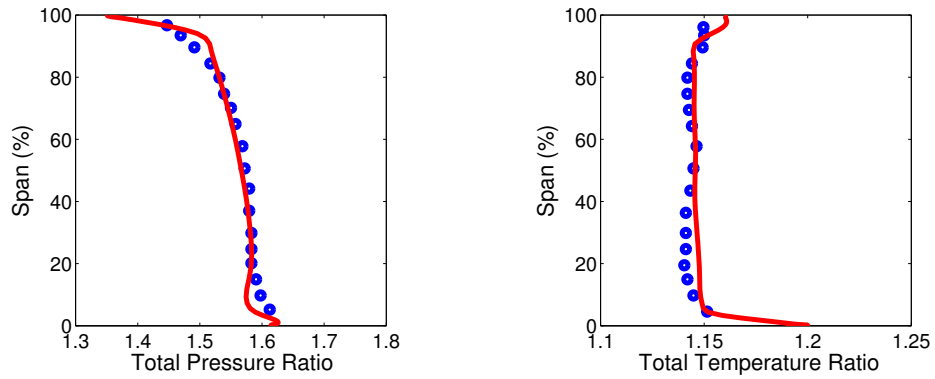
(b) 80% speed

(c) 60% speed

Figure 9: Total pressure ratio and temperature ratio distributions downstream of rotor, at high flow conditions (Blue: experimental data; Red: CFD solutions)

was the only fluctuation observed which shows the periodicity in one rotor rotation. There are 36 spikes which indicate 36 rotor blades passing the same sensor in one rotor revolution. In Figure 11, the dominant frequency is the blade-passing frequency (BPF). The time averaged values of the main flow parameters from the solution of this case were also compared with the steady state results. The maximum difference was less than 0.2%. This also provided confidence to perform the unsteady simulation at near stall condition.
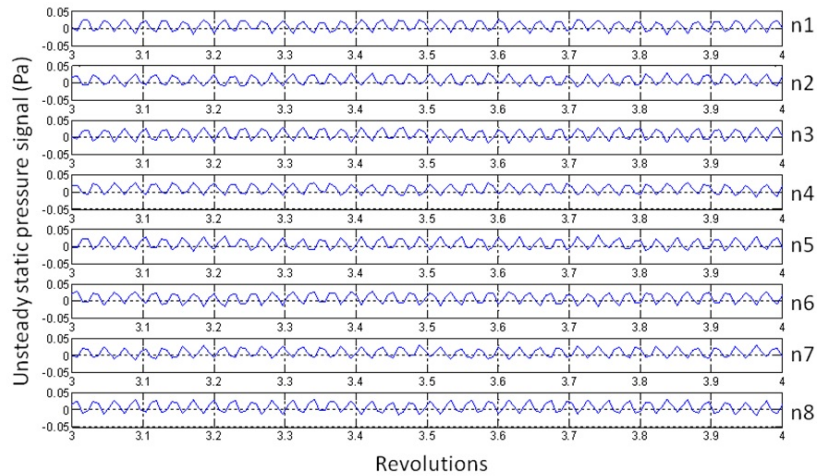

Figure 10: Unsteady static pressure time history at the inlet of rotor without rotating stall

5.2. Unsteady calculations near stall

For the damaged blade study, the investigation was carried out on assemblies with different degrees of one damaged blade and multiple damaged blades. The aim was to investigate their effects on compressor performance
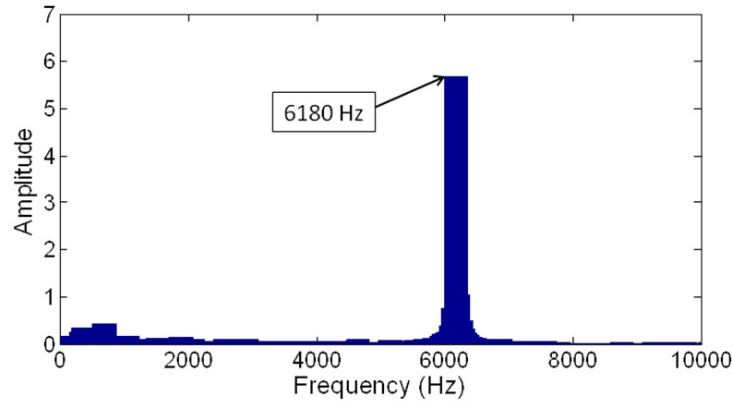
18

Figure 11: Fourier transform components from one of the numerical sensors on the casing

and flow behaviour when the compressor was operating near stall boundary. Two different degrees of damaged blades were used as shown in Figure 12. Each damage starts at the leading edge to 20% of chord on the tip and from 70% span increasing its spanwise extent linearly up to the tip forming a typical tip curl damage.

Before considering blade damage effect, it is useful to examine the flow behaviour and rotating stall characteristics for a case without damaged blades. It is important to identify a methodology to initiate rotating stall without excessive computational time. It is well known that in actual geometries there are small manufacturing tolerances which are believed to contribute to the onset of rotating stall at specific locations in an assembly. Computational domains resulting from repeating a single passage mesh are, however, perfectly symmetric. Previous numerical simulations on those geometries, expected to experience rotating stall, showed that rotating stall simulations

19
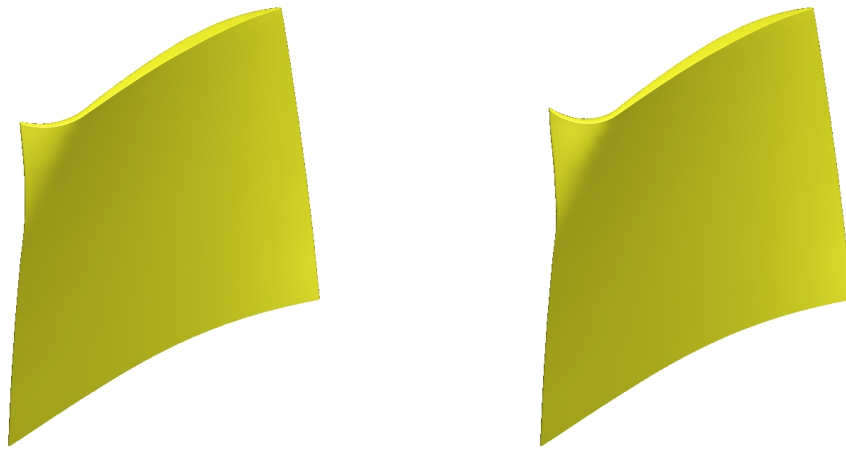
(a) Medium damage

(b) Heavy damage
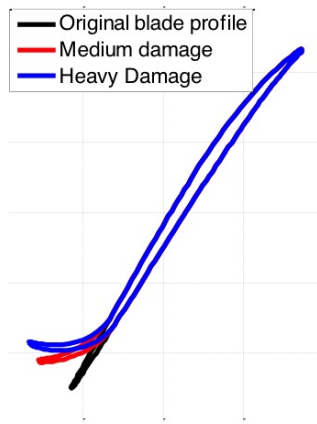
(c) 2D blade profile comparison near the tip

Figure 12: Curl damage at leading edge

are possible. It is likely that accumulated round off errors eventually lead to some differences among passages leading to the onset of stall at specific locations. However, that requires the simulation of many rotor revolutions before the onset of rotating stall happens. It was also found that introducing small asymmetry of the same order of manufacturing tolerances could lead to a much quicker onset of rotating stall in the numerical simulations and

significant computer time savings. Therefore, all blades in the computational domain were randomly staggered between -0.2^o and 0.2^o to create the required asymmetry. As reported by Vahdati et al. [19], a larger variation of stagger pattern was used and it was verified that the results were not affected regardless of the pattern used.

One operating point (rotor speed: 10313.2 rpm, mass flow: 10.09 kg/s) was chosen for all unsteady simulations. This point was the near stall point obtained from steady state simulations which was used as an initial solution for the unsteady simulation. The unsteady simulation of one rotor revolution requires about 25 hours using 32, 2.5 GHz Intel Xeon cores. 1350 time steps per rotor rotation were used for all unsteady simulations reported in this paper. The unsteady simulation without damaged blades will be discussed first.

5.2.1. Rotating stall for undamaged assembly

The overall compressor performance during rotating stall for this case is shown together with the steady state solution in Figure 13. The unsteady mass flow rate was obtained in the last 10 revolutions. The time averaged mass flow rate with rotating stall was similar to the near stall point from the steady state solution but the pressure ratio decreased by approximately 1%. Figure 14 shows a comparison of the circumferentially averaged axial velocity profile downstream of the rotor. It can be seen that from about 75% span to the casing, the average axial velocity during rotating stall is higher than

that obtained from the steady state solution with no stalled cells. Further investigation of the detailed flow behaviour allows explaining this. Figure 15 shows Mach number contour comparison at 75% span. It can be seen that downstream the unstalled passages, the Mach number is higher than that in the steady simulations due to the low or negative incidence. This indicates higher mass flow through unstalled passages in the upper part of the passage, which appears to compensate for the mass deficit in the stalled regions and the lower part of the passage.
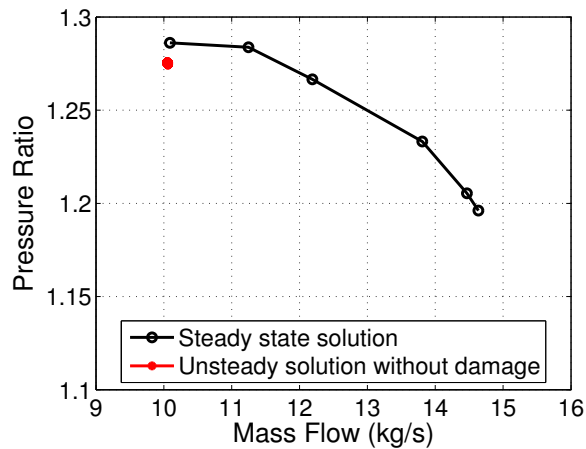

Figure 13: Compressor performance during rotating stall with steady state solutions

5.3. Unsteady calculations near stall

As seen in the full time history from numerical sensors in Figure 16a, after the initial numerical transient, three different types of spikes can be observed which indicate three different patterns of stall cells. Rotating stall started approximately after the 8th revolution. After a long transition period, a
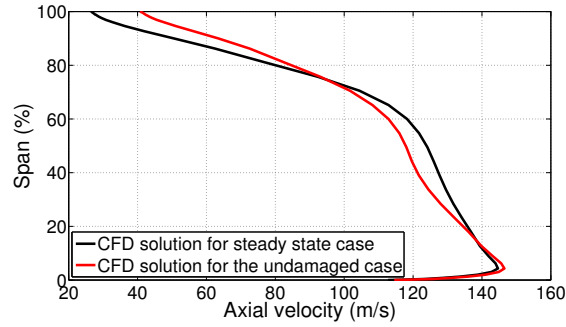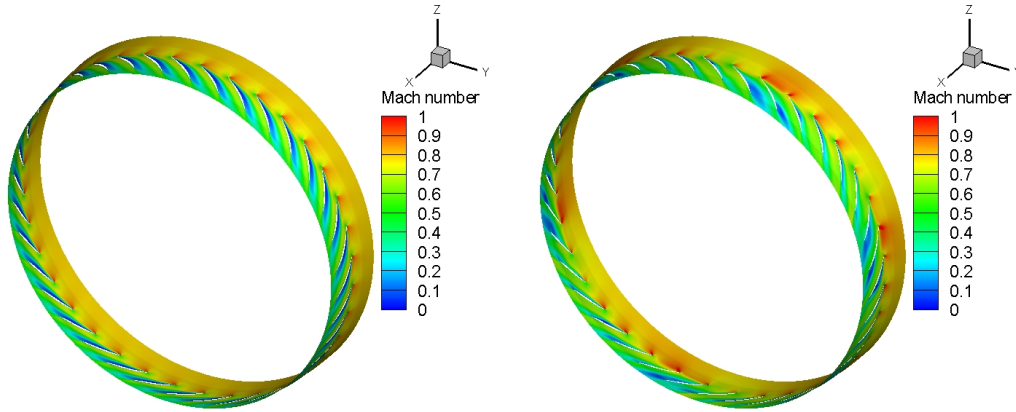
22

Figure 14: Circumferentially averaged axial velocity profile comparison downstream the rotor


(a) Steady state   (b) Undamaged case

Figure 15: Mach number contour comparison at 75% span of the rotor

regular pattern was formed at around the 40th revolution with 6 stall cells. It can be seen that 5 spikes representing 5 rotating stall cells passed the same sensor in Figure 16b in one engine revolution. Therefore, the propagation speed of rotating stall cells could be worked out which was 83% of rotor speed. This information could also be worked out from Figure 17. Three main frequencies are shown: BPF, frequency of rotating stall and its second

23

harmonic.
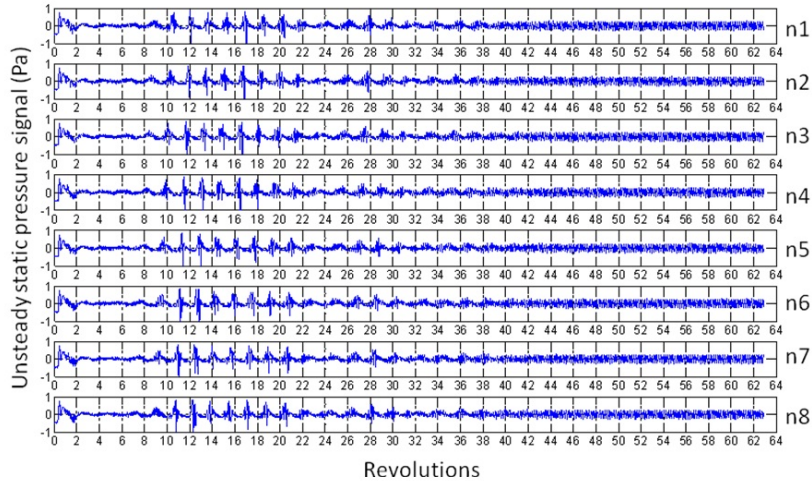
(a) Full time history
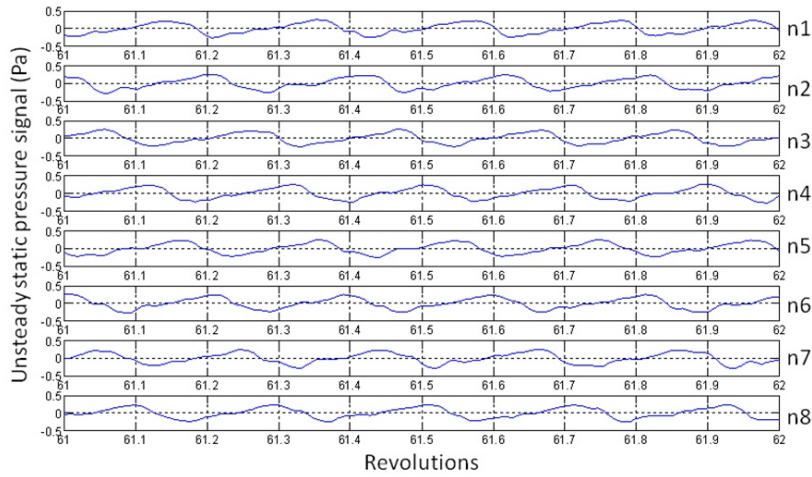
(b) Time history in one rotor revolution

Figure 16: Unsteady static pressure time history from numerical sensors on the casing for the undamaged assembly

For the flow behaviour during rotating stall, the instantaneous negative axial velocity near the tip of the rotor is shown in Figure 18. It was obtained after a regular rotating stall pattern was formed. Six stall cells were found
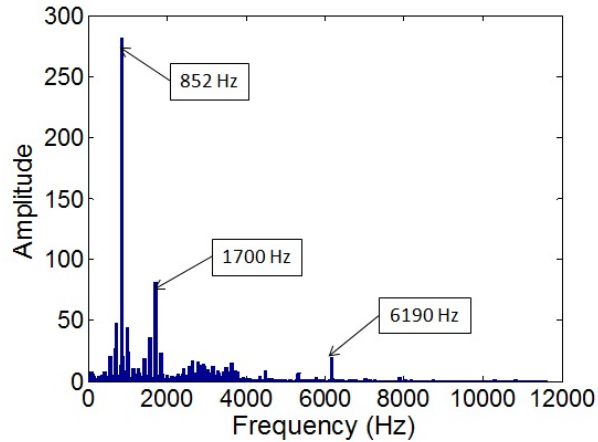
24

Figure 17: Fourier transform components of numerical sensor 7 on the casing

with similar size and approximately equally spaced. Each of them covered about 60% of the axial domain in the rotor. Rotating stall for this rotor at design speed was investigated using multi-passage model [20]. For that case, rotating stall predicted also has 6 stall cells with a propagation speed of 80% of the rotor speed based on the available data. Stall cells covered about 40% span of rotor blades and about 4 passages in the circumferential direction. The spanwise extent of rotating stall is larger than the present study and could be caused by the interaction between shock waves, boundary layer and tip clearance flow at design speed while present predictions are performed at 60% of the design speed. In addition, their simulations were performed over two engine revolutions only and the solution could have developed to a different pattern if the simulations were continued beyond that. Figure 19 shows the negative axial velocity on an axial cut in the rotor at the same time instant as in Figure 18. The axial cut plane is at 40% of chord

length downstream from the leading edge at the hub. It also shows stall cells equally spaced in the circumferential direction and covered about 17% in radial span. This shows that stall cells are found only near the tip region. That is a typical behaviour of spike type rotating stall as reported by Day [21] which shows that stall cells tend to be confined to the tip region of the rotor suggesting that tip clearance flow is mostly responsible for its inception. Spike type disturbances have also been experimentally measured to have a circumferential extent of two to three blade passages ([21], [22], [23]).
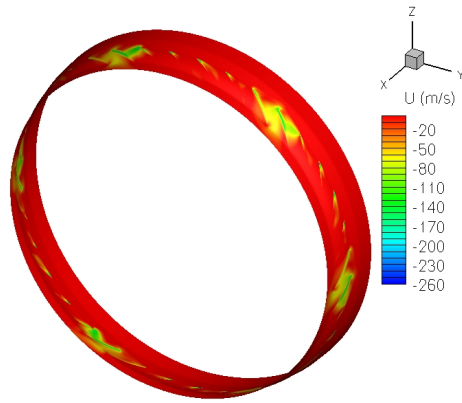

Figure 18: Instantaneous negative axial velocity near the tip of the rotor

Figure 20 shows 3D streamlines contoured by the negative axial velocity. The inflow comes from the leading edge of one blade, and the back flow was reversed at the trailing edge of the neighbouring blade and going into the passage. It meets the tip clearance flow and the vortex of the stall cell. The interface between the streamwise inflow and with tip clearance flow is aligned with the leading edge plane. This is consistent with the explanation
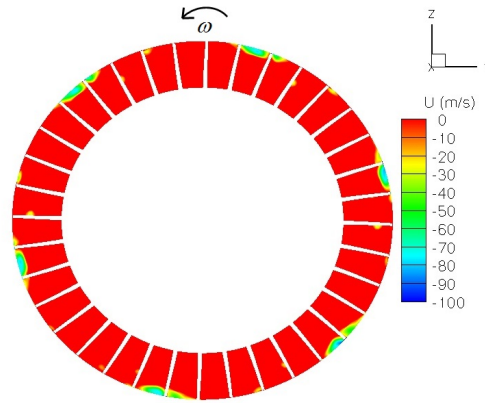
26

Figure 19: Instantaneous negative axial velocity on an axial cut plane

of the flow features for the spike initiated rotating stall proposed by Vo et al [3]. Inside the stall cell the blocked flow diverts the oncoming flow to the neighbouring area. Outside the stall cell, flow is passing the passages smoothly without blockage. Stall cell also formed a radial vortex attached to the blade and the casing. The concept of radial vortex was proposed by Inoue et al. [24] and also recently confirmed by Weichert et al. [25] and Pullan et al. [26]. The similarity predicted in this study is due to the design of this rotor, some blades encounter higher incidence beyond the critical value near the tip region which leads to separations from the suction side. The stalled region constitutes a radial vortex attached to the suction side and the casing. As shown in Figure 20 in the rotor reference frame, when the cell is propagating in the anti-clockwise direction, the vortex leaves the suction side of one blade and moves towards the pressure side of the next blade, which will divert the flow to the surrounding region. Also the stall cell indicates a

27

pressure building up which forms the spike in the unsteady pressure signal time history. This is different from the stall pattern found by Pullan et al. [26], who predicted a radial vortex starting from the blade's leading edge at the suction side which could be due to the different compressor blade design used in their analysis where the blades have lower hub to tip ratio and thus rotor blades have much less twist near the tip than Rotor 37.
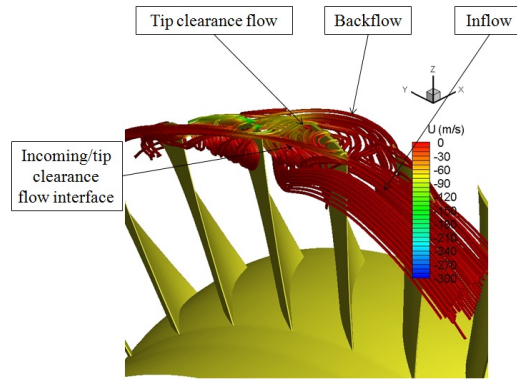

Figure 20: 3D stream trace inside the stall cell

5.3.1. Rotating stall with one damaged blade

In this subsection the comparison of one damaged blade with different degrees of damage is discussed. The case with one medium damaged blade and one heavy damaged blade will be noted as Damaged Case 1 and Damaged Case 2 respectively. A comparison of compressor performance is shown in Figure 21. For Damaged Case 1, the overall compressor performance was very similar for the mass flow but the pressure ratio decreased slightly compared to the undamaged case, which could be caused by rotating stall with the damaged blade. Compressor performance for Damaged Case 2 has

28

slightly larger variation for mass flow and pressure ratio than Damaged Case 1. However, both cases do not have significant influence on the overall compressor performance. The reason for that is the same as for the undamaged case, the results are similar as shown in Figures 14 and 15. Therefore, they are not shown here to avoid repetition.
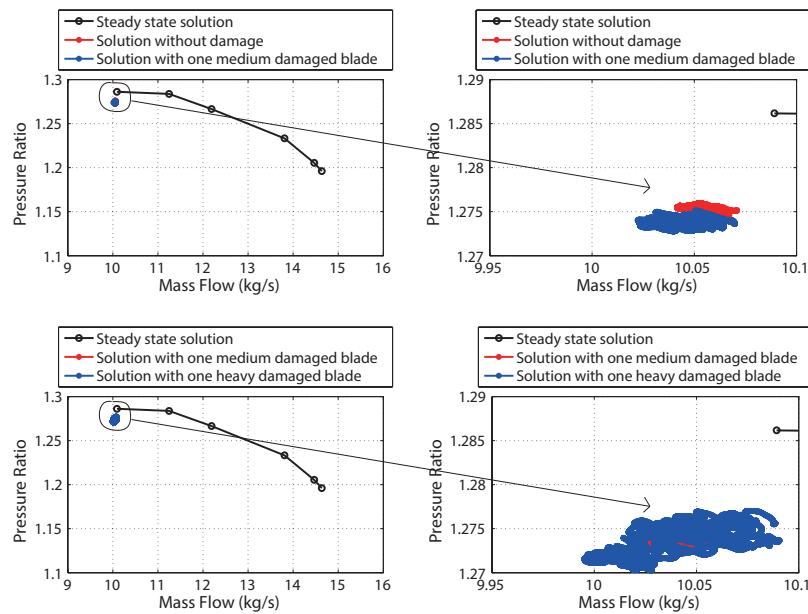

Figure 21: Compressor performance during rotating stall with one damaged blade

It was observed that stall cells started from the damaged blade and rotated in the opposite direction to rotor rotation seen in the relative frame. For Damaged Case 1 in Figure 22a, after the initial numerical transit, rotating stall started after 2 revolutions. Then the transition process of 28 revolutions took place untill a clear pattern was established after the 30th revolution. Compared to the undamaged case, it takes less time to achieve a clear form

of rotating stall. It can be seen from Figure 23a that when increasing the damage, it takes longer for the flow to settle. In Figures 22b and 23b, it can be seen that 5 and 6 cells passed the same sensors in that time period for Damaged Case 1 and Damaged Case 2 respectively. There are small kinks at the beginning of some of the spikes for both cases with damage, circled on the plot. That could be the effect that the cell just passed the damaged blade. Compared to the undamaged case, the rotating stall characteristic is the same for Damaged Case 1. For the Damaged Case 2, there are 7 rotating stall cells instead. The propagation speed of rotating cells is very similar to the other two unsteady cases.

Figure 24 shows the instantaneous negative velocity near the tip. For both cases with damage, 6 and 7 rotating cells could be observed respectively at the same time with similar size, shape and approximately equally spaced. Compared with the undamaged case, the difference is that a non-rotating stall cell covered the neighbouring region around the damaged blade all the time after rotating stall started. It is caused by the presence of the damage, which always diverts the flow. When a rotating stall cell passes through the damaged blade passage, it merges with the non-rotating cell. After it passes by, the non-rotating cell recovers to its original state. That could be seen clearly in the animation. The extent of stall cells in the radial direction can be seen in Figure 25, which shows the negative axial velocity on an axial cut plane at 40% chord downstream from the leading edge at the hub. For Damaged Case 1, each stall cell covered the same extent as the undamaged
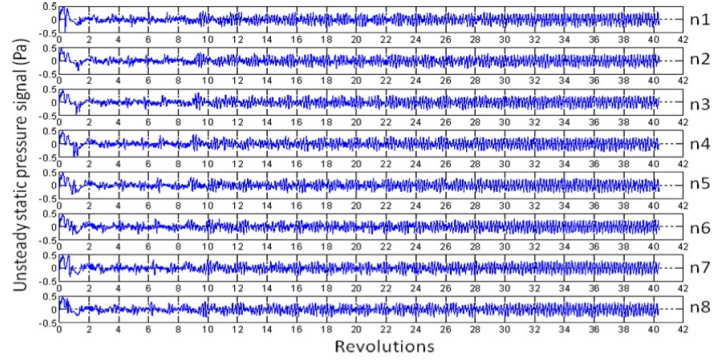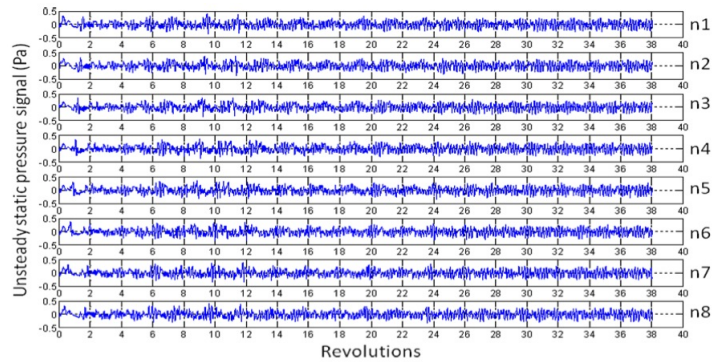
(a) Full time history for Damaged Case 1
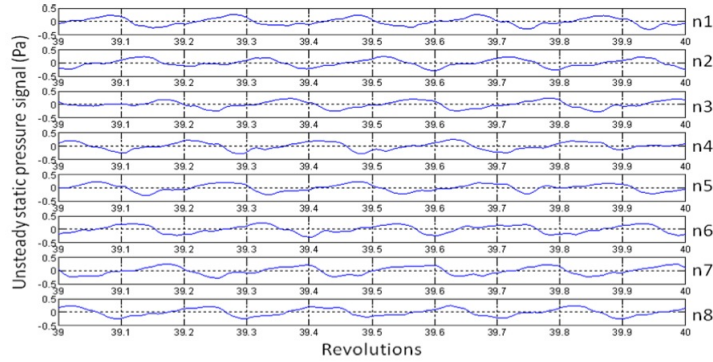
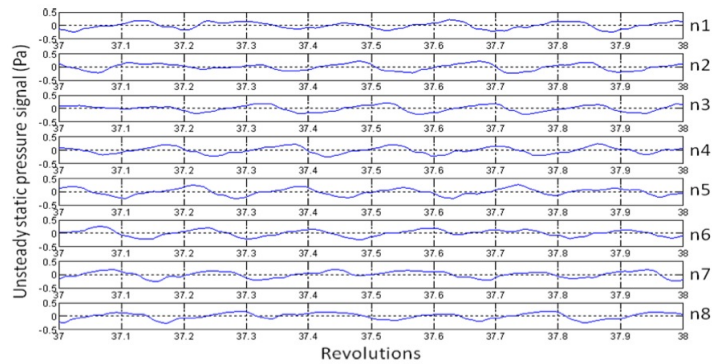(b) Time history in one revolution for Damaged Case 1

Figure 22: Unsteady static pressure signal time history from numerical sensors on the casing for Damaged Case 1

case. The non-rotating stall cell is smaller in the radial direction covering about 11% of the blade span. For Damaged Case 2, the rotating cells covered from about 10% to 18% of the span and non-rotating cell covered about 12%.

Figure 26 shows 3D structure of stall cells after a clear rotating stall pattern obtained for Damaged Case 1. Figure 26a shows the non-rotating stalled region including the damaged blade. Figure 26b which is obtained at a consequent time to Figure 26a shows one stall cell was merging with the non-rotating stall cell. The size of the stalled region enlarged in both

31

(a) Full time history for Damaged Case 2

(b) Time history in one rotor revolution for Damaged Case 2

Figure 23: Unsteady static pressure signal time history from numerical sensors on the casing for Damaged Case 2

radial and circumferential directions. When rotating cells passed the non-rotating stall region, the structure of the non-rotating stall region recovers after rotating cell passes by as mentioned earlier. The structures of other cells at other locations seem to be very similar as in the undamaged case. Again, it showed that the non-rotating stall cell was caused by the damaged blade because the flow was always diverted by the damage feature at the leading edge. For Damaged Case 2, the difference is that the non-rotating stall cell is
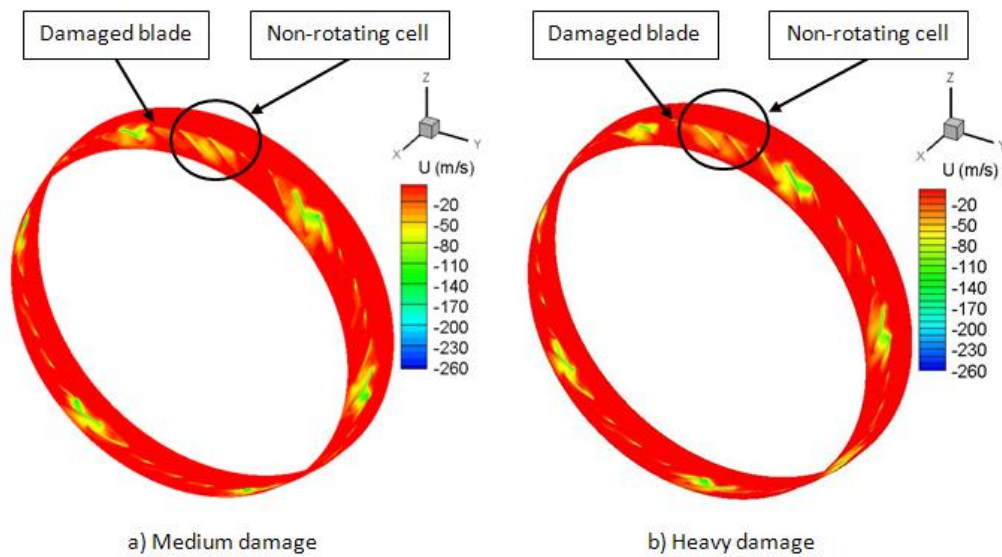
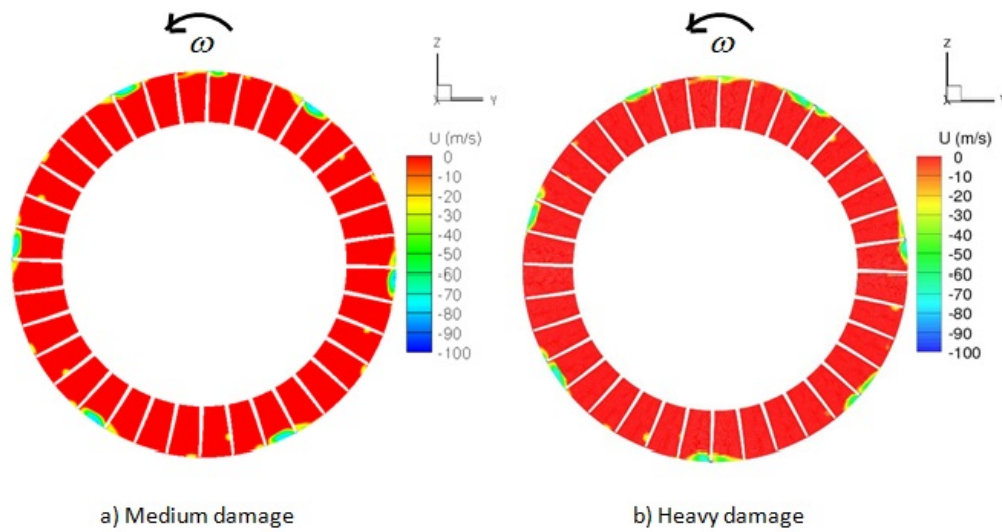Figure 24: Instantaneous negative velocity near the tip of the rotor

Figure 25: Instantaneous negative velocity on an axial cut plane

slightly larger in all extent. It can be concluded that both Damaged Case 1 and Damaged Case 2 do not have noticeable effect on the overall compressor performance. The characteristic of rotating stall differs slightly in the number

33

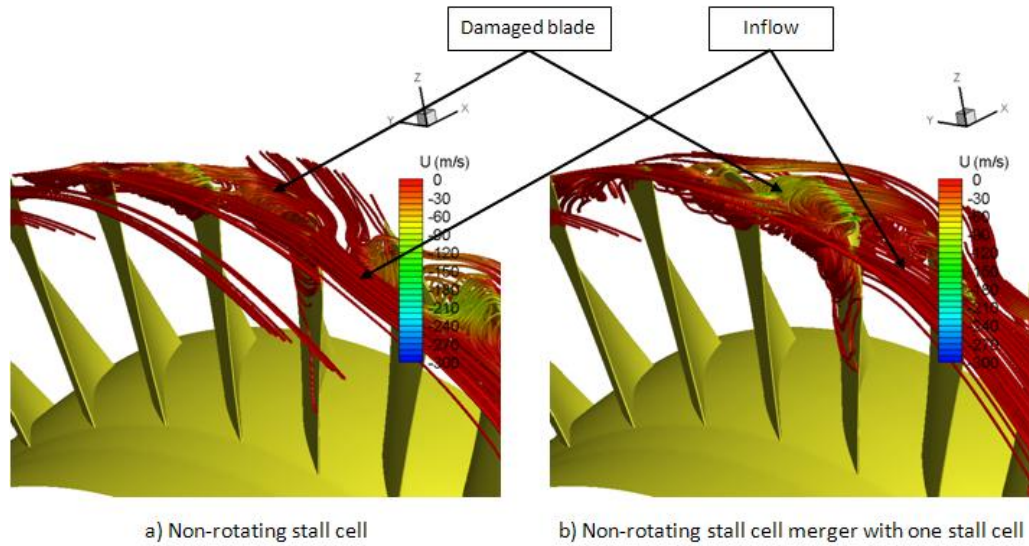of stall cells and the extent of the non-rotating stall cell.

Figure 26: Stall cell structure for Damaged Case 1

5.3.2. Rotating stall with multiple damaged blades

The last case investigated was a rotor assembly with six damaged blades of medium degree of damage. This case will be labelled as Damaged Case 3. The rotor assembly used is partially shown in Figure 27. The six damaged blades were allocated next to each other for the reason that it was believed that it was likely to provide the most negative effect on compressor performance with this arrangement.

Figure 28 shows a comparison of overall compressor performance with steady state simulation during the last 10 revolutions of the simulation. Compared to the steady state solution, the mass flow was very similar and on the other hand the pressure ratio had a slightly larger reduction, which was
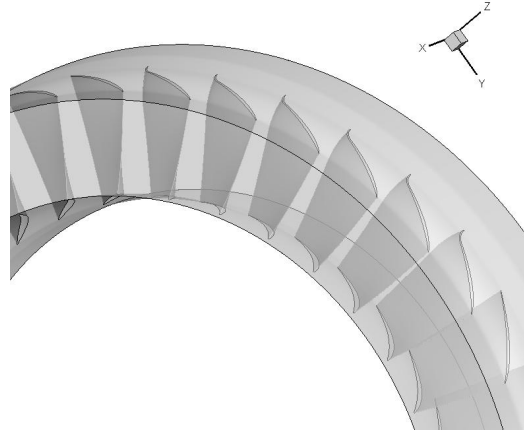
Figure 27: Part of the rotor assembly for Damaged Case 3

about 1.2%. Compared to other unsteady cases, mass flow has large varia-
tion. However, it could also be seen that there was no significant change on
the compressor overall performance. This case does not have a clear pattern
of rotating stall and it is believed that it will not have one. Due to the limited
time scale for this study, it is not possible to prove at this stage.
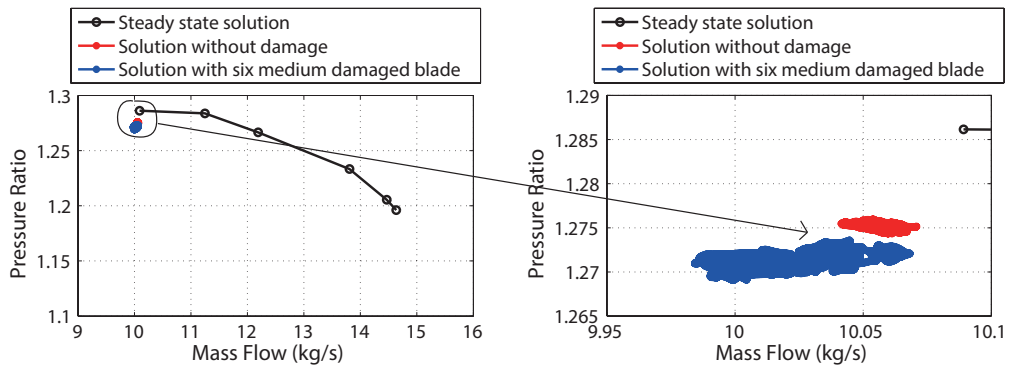

Figure 28: Compressor performance for Damaged Case 3

Figure 29 shows the unsteady static pressure signal time history from

numerical sensors. The case was simulated more than 90 revolutions with the mass flow still changing. That indicates that with six damaged blades in the rotor assembly, it could take a much longer time for the flow to settle. In Figure 29b, the rotating stall pattern was very different from other cases. There was rotating stall cell passing the large non-rotating stall region, which was circled in the plot.
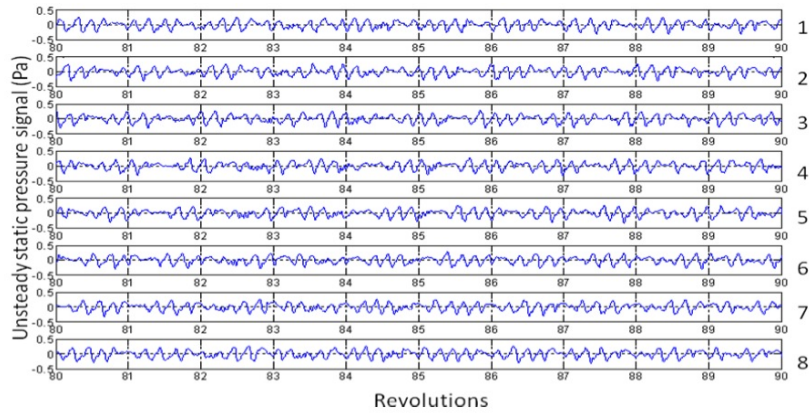
(a) Time history in 10 revolutions
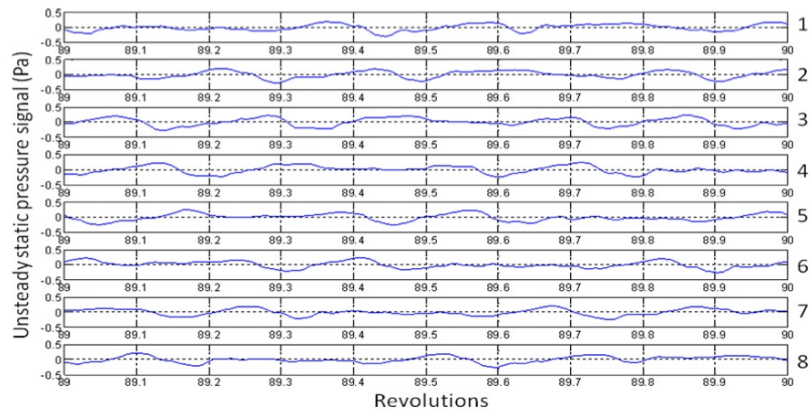
(b) Time history in one rotor revolution

Figure 29: Unsteady static pressure signal time history from numerical sensors on the casing

36

Figure 30 shows the instantaneous negative axial velocity near the tip of the rotor and the contour plot was captured after the 91st revolution, which was close to the end of the simulation. There was a very large non-rotating stalled region covering the damaged blades and some of the neighbouring area, from the animation. In the meantime, there were three other cells in much smaller size which were propagating around the annulus. Another negative axial velocity contour plot was obtained on an axial cutting plane, which was 40% of chord length downstream, the leading edge of the rotor on the hub in Figure 31. As clearly seen from the plot, the large non-rotating stalled region covered about 9 blade passages and three smaller cells covered about two passages each and up to 17% of the radial span. Since the flow is still changing, it was difficult to determine the propagation speed of stall cells.
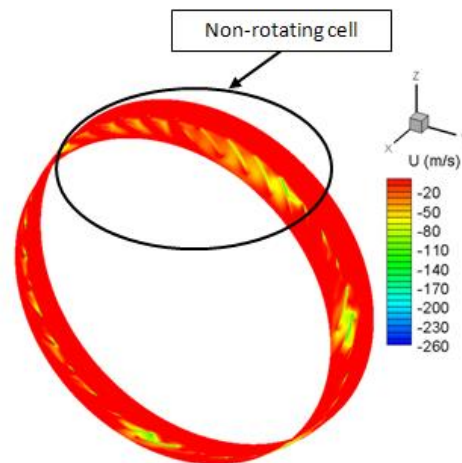

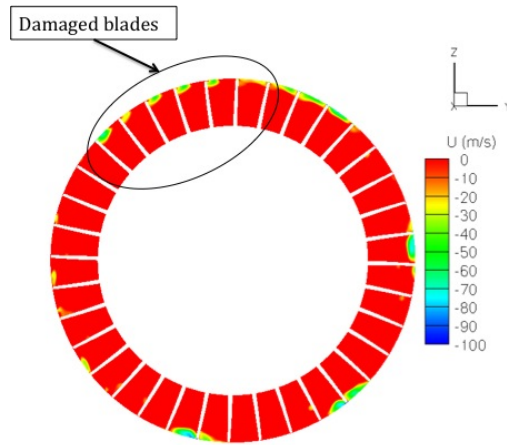Figure 30: Instantaneous negative axial velocity near the tip of the rotor

Figure 31: Instantaneous negative velocity on an axial cutting plane through the rotor blade

6. Conclusions

A compressor rotor assembly with three different blade damage patterns was simulated. The undamaged assembly was also simulated for comparison. Spike type initiated rotating stall was predicted in all cases and the corresponding flow features were found to be similar to those reported in the literature. The assembly with one medium damaged blade had a similar stable and clear rotating stall pattern to the undamaged assembly except for one additional non-rotating stalled region caused by the damaged blade. When increasing the degree of damage of one blade, spike type rotating stall was found as well but with a different pattern. Both the number of stall cells and the non-rotating stalled region were increased. In the case with multiple damaged blades with identical medium damage, a large stationary stalled region was found which covered approximately quarter of the annulus

38

and three other smaller stall cells rotated around the annulus. It was found that it is more difficult for the flow to settle to a regular pattern when the degree of damage or number of damaged blades is increased. For all cases with rotating stall except the one with multiple damaged blades, mass flow was not significantly affected compared to steady-state simulations because the flow deficit was compensated by increased flow in the unstalled passages.

For one damaged blade with two different degrees of damage the stall cells rotated in the same direction of rotor rotation with a propagation speed about 83% of the shaft speed. Stall cells were approximately equally spaced and covered two rotor passages in the circumferential direction and about 17% of the passage in the spanwise direction. The flow features regarding the radial vortex and its propagation mechanism conforms to those reported in the literature for undamaged assemblies.

Contrary to expectation, tip curl damage investigated did not have significant effects on compressor overall performance near stall. This result may not be generalised and further investigations of different damage patterns are required to make firm conclusions. Since the unsteady full annulus simulations require extensive computational resources, it was not possible to perform a detailed parametric study to find the degree of damage, which would have detrimental aerodynamic effects on the compressor.

References

[1] Greitzer, E. M., "The stability of pumping systems-The 1980 Freeman Scholar Lecture", *ASME J. Fluids Eng.*, Vol. 103(2), pp.193-242, (1981).

[2] de Jager, B., "Rotating stall and surge control: A survey", *Proceedings of the 34th Conference on Decision & Control*, (1995).

[3] Iura, T. and Rannie, W. D., "Experimental investigations of propagating stall in axial-flow compresors", *Transactions of ASME*, Vol. 76, pp. 463-471, (1954).

[4] Vo, H. D., Tan, Ch. S. and Greitzer, E. M. "Criteria for spike initiated rotating stall", *ASME: Journal of Turbomachinery*, Vol. 130, (2008).

[5] Levine, P., "Axial compressor performance and maintenance guide", *Electric Power Research Institute, Inc.*, (1998).

[6] Kim, M., Vahdati, M. and Imregun, M. "Aeroelasti stability analysis of a bird-damaged aeroengine fan assembly", *Aerospace Science and Technology*, Vol. 5, pp. 469-482, (2001).

[7] Frischbier, J. and Kraus, A. "Multiple stage turbofan bird ingestion analysis with ALE and SPH methods", *MTU Aero Engines GmbH ISABE-2005*, D-80976 Muenchen, Germany, (2005).

[8] Meguid, S. A., Mao, R. H. and Ng, T. Y. "FE analysis of geometry ef-

fects of an artificial bird striking an aeroengine fan blade", *International Journal of Impact Engineering*, Vol. 35, pp. 487-498, (2008).

[9] Guan, Y., Zhao, Zh., Chen, W. and Gao, D. "Foreign object damage to fan rotor blades of aeroengine Part II: Numerical simulation of bird impact", *Chinese Journal of Aeronautics*, Vol. 21, pp. 328-334, (2008).

[10] Dhandapani, S., Vahdati, M. and Imregun, M. "Forced response and surge behaviour of IP core-ompressors with ice-damaged rotor blades", *Proceedings of ASME Turbo: Power for Land, Sea and Air*, GT2008-50335, (2008).

[11] Bohari, B. and Sayma, A. I. "CFD analysis of effects of damage due to bird strike on fan performance", *Proceedings of ASME Turbo Expo: Power for Land, Sea and Air*, GT2010-22365, (2010).

[12] Denton, J. D. "Lessons from Rotor 37", *Journal of Thermal Science*, Vol. 6, pp1-13, (1996).

[13] Sayma, A. I., Vahdati, M., Sbardella, L. and Imregun, M. "Modelling of 3D viscous compressible turbomachinery flows using unstructured hybrid grids", *AIAA Journal*, Vol. 38, pp. 945-954, (2000).

[14] Sayma, A. I. "Towards virtual testing of compression systems in gas turbine engines", *The NAFEMS International Journal of CFD Case Studies*, (2009).

[15] Suder K. L. "Blockage development in a transonic axial compressor rotor", *NASA TM-113115*, (1997).

[16] Vahdati, M., Sayma, A. I., Freeman, C. and Imregun, M. "On the use of atmospheric boundary conditions for axial-flow compressor stall simulations", *Journal of Turbomachinery*, Vol. 127, pp. 349-351, (2005).

[17] Wu, X., Vahdati, M., Sayma and Imregun, M. "A numerical investigation of aeroacoustic fan blade flutter", *Proceedings of ASME Turbo Expo 2003*, GT2003-38454, (2003).

[18] Choi, M., Smith, N. H. S. and Vahdati, M. "Validation of numerical simulation for rotating stall in a transonic fan", *Proceedings of ASME Turbo Expo*, GT2011-46109, (2011).

[19] Vahdati, Simpson, G. and Imregun, M. "Unsteady flow and aeroelasticity behaviour of aeroengine core compressors during rotating stall and surge", *Journal of Turbomachinery*, Vol. 130, pp. 031017-1-031017-9, (2008).

[20] Zhang, Y., Lu, X., Chu, W. and Zhu, J. "Numerical investigation of the unsteady tip leakage flow and rotating stall inception in a transonic compressor", *Journal of Thermal Science*, Vol. 19, pp. 310-317, (2010).

[21] Day, I. J. "Stall inception in axial flow compressors", *ASME Journal of Turbomachinery*, Vol. 115, pp. 1-9, (1993).

[22] Silkowski, P. D. "Measurements of rotor stalling in a matched and mismatched multistage compressor", *Massachusetts Institute of Technology*, GTL Report No. 221, (1995).

[23] Day, I. J. and Freeman, C. "The unstable behaviour of low and high speed compressors", *ASME Journal of Turbomachinery*, Vol. 116, pp. 194-201, (1994).

[24] Inoue, M., Kuroumaru, M., Tanino, T., and Furukawa, M. "Propagation of multiple short-length-scale stall cells in an axial compressor rotor", *ASME Journal of Turbomachinery*, Vol. 122, pp. 45-54, (2000).

[25] Weichert, S. and Day, I. "Detailed measurement of spike formation in an axial compressor", *Proceedings of ASME Turbo Expo*, GT2012-68627, (2012).

[26] Pullan, G., Young, A. M., Day, I. J., Greitzer, E. M. and Spakovszky, S. "Origins and structure of spike-type rotating stall", *Proceedings of ASME Turbo Expo*, GT2012-68707, (2012).